Modeling instrumented test articles for Plasmatron X aerothermal environment

Sreevishnu Oruganti*, Sanjeev Kumar†, Vincent Le Maout‡, Lorenzo Capponi§, Alessandro Munafò¶, Daniel J. Bodony‖, Marco Panesi**, and Francesco Panerai††
Center for Hypersonics and Entry Systems Studies
University of Illinois at Urbana-Champaign, Urbana IL

Nagi N. Mansour‡‡ and Sergio Fraile Izquierdo§§
AMA Inc. at NASA Ames Research Center, Moffett Field, CA 94035, USA

This work discusses the ablative response of thermal protection system materials when exposed to aerothermal environments. It focuses on modeling instrumented test article assemblies tested in the Plasmatron X inductively coupled plasma wind tunnel. For this purpose, as the samples are mounted to a water-cooled arm using numerous assembly components and are embedded with thermocouples for in-depth temperature measurements, the variation in ablative response of the samples as a result of these components is studied. The aerothermal boundary conditions for Plasmatron X are obtained for hypersonic flight-relevant conditions using the multi-physics aerothermal framework built at the University of Illinois at Urbana-Champaign. For simulating the material response, a material response code, Porous Material Analysis Toolbox based on OpenFOAM (PATO) is used. In PATO, numerous configurations and materials of thermocouples were studied. The optimal configuration for obtaining temperature measurements with minimal error using embedded thermocouples was found to be the U-shaped Type S, 30 American wire gauge thermocouple configuration.

I. Introduction

To assess thermal protection system (TPS) materials performance in hypersonic applications, ground testing is performed in high-enthalpy facilities, such as arc-jets and Inductively Coupled Plasma (ICP) torches [1, 2]. In ICP facilities, a high-temperature plasma is generated by coupling high-power radio frequency energy to a jet of pressurized gas, heating the gas to extreme temperatures and forming plasma. The plasma jet is then accelerated by means of a nozzle and evacuated into the test section at high speeds. A TPS material sample mounted on a water-cooled arm is then inserted into the plasma flow to investigate the response of the material. The heat flux and stagnation pressure experienced by the sample at the stagnation point are chosen to correlate with entry conditions [3]. The objective of testing in the ICP is to characterize the response of the material and assess the performance of the TPS material [1].

Experimental constraints imposed by the facility require the assembly of a stack of components that form the testing probes. These include the TPS sample being tested, the sample holder (usually graphite), insulator and fixtures. The presence of different materials and their contact to water-cooled surfaces could substantially affect the internal temperature of the test sample. In addition, samples are instrumented with thermocouples at various depths to investigate the thermal response of the material to the high-enthalpy environment. As thermocouple wires have substantially different thermal properties than porous material, and are in contact with water-cooled surfaces, they act as heat sinks. This effect can locally affect the measured in-depth temperature and pressure of the TPS material [4, 5]. This leads to a local difference in the material temperature between the non-instrumented material as used in hypersonics applications

*PhD candidate, Department of Aerospace Engineering, AIAA Member
†PhD Candidate, Department of Aerospace Engineering, AIAA Member
‡Postdoc Research Associate, Department of Aerospace Engineering, AIAA Member
§Postdoc Research Associate, Department of Aerospace Engineering
¶Research Scientist, Department of Aerospace Engineering, AIAA Member
‖Professor, Department of Aerospace Engineering, AIAA Member
**Professor, Department of Aerospace Engineering, AIAA Member
††Assistant Professor, Department of Aerospace Engineering, AIAA Associate Fellow
‡‡Adjunct Professor, Center for Hypersonics and Entry Systems Studies, AIAA Associate Fellow
§§Research Scientist, Analytical Mechanical Associates Inc. at NASA Ames, AIAA Member

and the test sample. Therefore, in order to accurately characterize the response of TPS materials, both the aerothermal heating effects from the flow and the effects due to the presence of the assembly components and thermocouples need to be evaluated.

In this work a test article assembly designed for the Plasmatron X facilitiy at the University of Illinois at Urbana-Champaign is modeled. Plasmatron X is a new 350 kW ICP wind tunnel facility designed and engineered by Tekna Plasma Systems, Inc. (Sherbrooke, QC, Canada), used to produce high-enthalpy flow of test gases that can mimic atmospheric entry conditions [6, 7].

The aerothermal environment on the sample in Plasmatron X is simulated for a given input power, chamber pressure and mass flow rate setting, using a multi-physics computational framework developed by Munafò et al. [8] for modeling inductively coupled plasma discharges. The framework consists of a CFD solver (HEGEL [9]) and an electromagnetic solver (FLUX [10, 11]), explicitly coupled using preCICE [12]. HEGEL is linked to a thermodynamic and transport properties library (PLATO [9]) for computing gas properties as well as kinetics source terms. The exchange of information within these solvers after each iteration is shown in Fig. 1. While the framework can be coupled with a radiation solver, MURP[13], this study does not consider radiation effects.

Simulation of aerothermal environment on the geometry of the test sample provide boundary conditions of species mass flux, heat flux, and stagnation pressure on the surface of the sample that are used as inputs for the material response solver, Porous Material Analysis Toolbox, based on OpenFOAM (PATO) [14]. PATO is a versatile state-of-the-art material response solver designed to simulate heat transfer, thermal decomposition and ablation of TPS materials. In this study, we simulate the thermal response of test samples and all the secondary components used in the assembly to mount and instrument them. Using this framework, different materials including pyrolyzing and non-pyrolyzing, porous and dense ablators are modeled. Additionally, characteristic thermocouple sizes and types used in actual test configurations are considered. The influence of the test assembly on the in-depth temperature is discussed, along with recommendations for test article design.

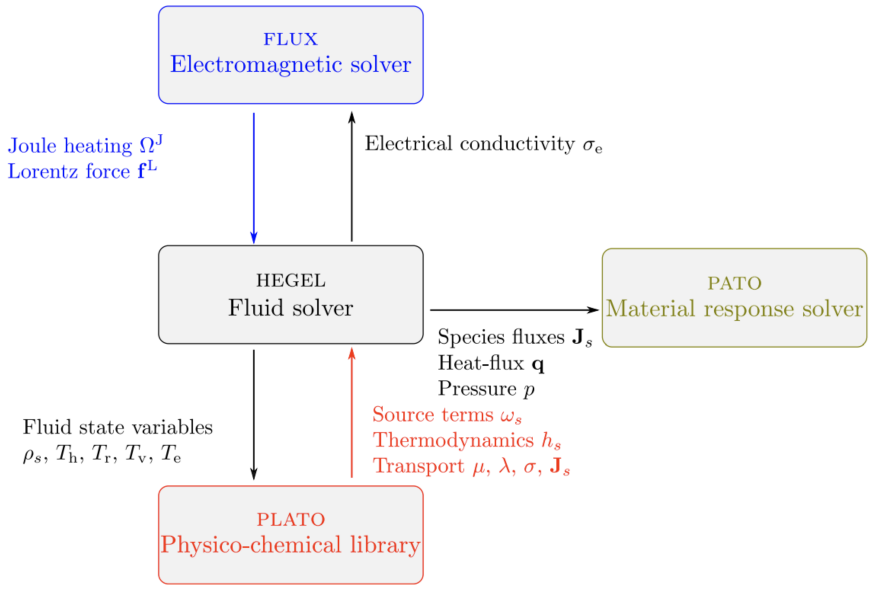

Fig. 1 Schematic illustrating the coupling framework between the solvers along with the variables being exchanged via preCICE.

In the paper, the methodology and simulation approach is described in § II, followed by simulation results obtained for the aerothermal environment in §III.A and material response in § III.B. Concluding remarks and future work are provided in § IV.

II. Methodology

A. Assembly Design

The isoQ shape is commonly used for evaluating TPS materials in aerothermal environments, due to its advantage in providing approximately uniform surface heat flux [15]. Samples with isoQ shape are attached to an insulator that connects to a holder, and mounted on a water-cooled arm that rotates the sample into the plasma flow. The insulator is used to reduce the cooling effects from the holder to the sample. Sample assemblies are also embedded with thermocouples to enable in-depth temperature measurements.

Based on these considerations, an assembly design was created for low- and high-thermal conductivity materials for testing in Plasmatron X. The assembly design consists of an isoQ shape material sample with a 2 cm diameter, a thermocouple plug of 1 cm diameter using the same material, a low-conductivity porous insulator made of zirconia, known as Zircar FBD (Zircar Zirconia Inc, Florida, NY, USA), a graphite disk, and a graphite holder (Bar-Lo Carbon Products Inc., Fairfield, NJ, USA). A schematic of the assembly is shown in Fig. 2. In this design, three thermocouples are embedded into the sample by means of a thermocouple plug inspired by the NASA Ames/MEDLI plug design[16]. The thermocouples are located at 5, 10, 15 mm depth from the stagnation point.

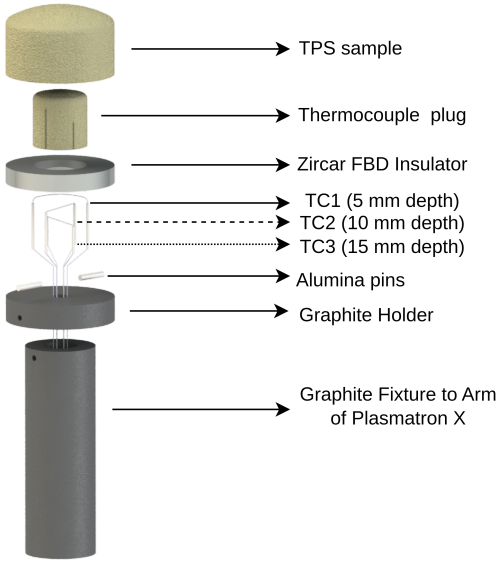

Fig. 2 Stack-up of assembly components used for TPS material testing in Plasmatron X.

To study the thermal response of the sample and the embedded thermocouples, the chosen assembly was simulated in PATO. As the primary goal of this study is to understand the performance of different embedded thermocouples of varying sizes and type, a detailed parametric study was conducted. Additionally, the TPS material properties were varied, in order to observe the variation in results as the properties of the TPS materials changed.

As a simplification to the mesh generation process, the two wires of the thermocouples were modelled as one with the average thermal properties of both wires. They were considered to have square cross-sections instead of circular ones. Additionally, the TPS sample and the thermocouple plug are modelled as a single block, in order to reduce mesh skewness near the interface between the sample and the plug due to recession. Finally, as a simplification, only one thermocouple located at 15 mm depth was simulated using different thermocouple configurations.

B. Computational Domain for Aerothermal Environment

A 2-dimensional axisymmetric structured grid was created using *Pointwise* to simulate the Plasmatron X flow field using the coupling framework described in Fig. 1. The computational domain was separated into numerous blocks to allow quality meshing for complex geometries. The torch section has a swirling central injection port, and a sheath injection port which are modelled accordingly. The straight 100 mm diameter torch is modelled for this study. In the

chamber, the sample assembly is placed at a 150 mm distance from the torch exit to the stagnation point of the sample. The diffuser, or catch cone, of the Plasmatron X is also included in the domain in order to capture possible effects of its presence in the facility.

To accurately resolve the boundary layer over the sample, mesh refinement was applied based on literature recommendations[17]. The final mesh had a cell spacing of 10^{-6} m, 5×10^{-5} m and 10^{-4} m at the stagnation region of the sample, back-wall of the sample, and torch walls, respectively. The dimensions of the Plasmatron X chamber and the grid are shown in Fig. 3.

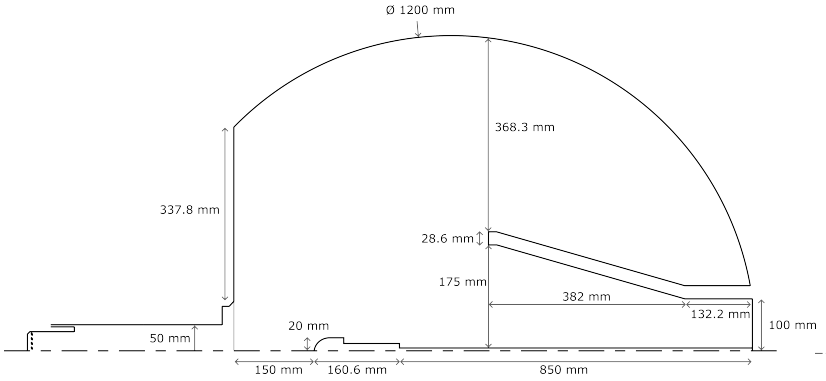

(a) Dimensions of test-section.

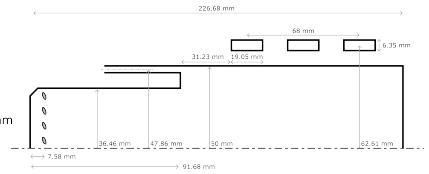

(b) Dimensions of torch section.

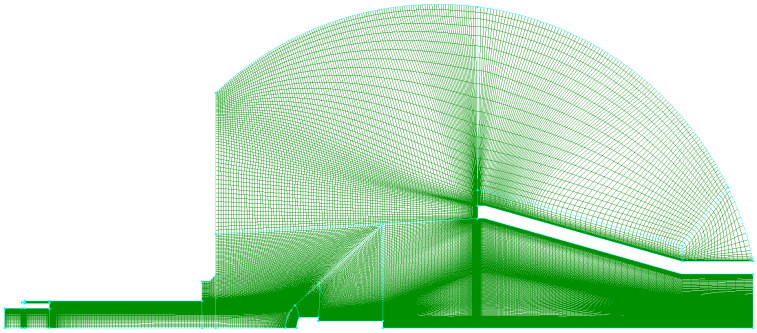

(c) Entire CFD domain

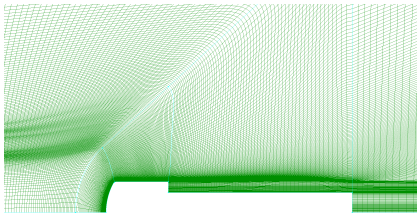

(d) Mesh near sample geometry.

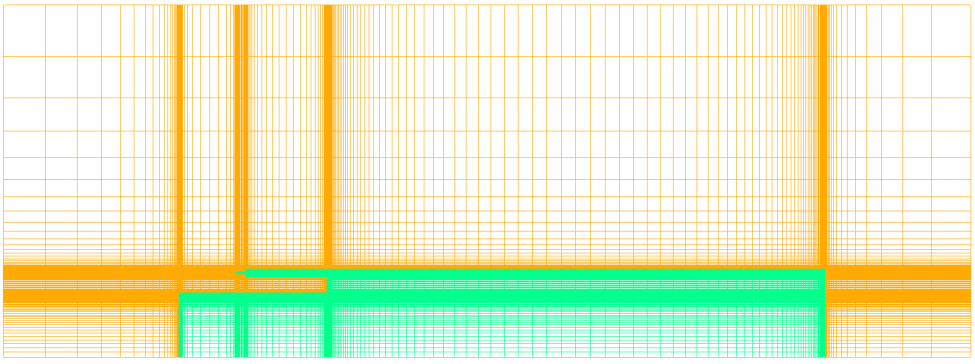

(e) Green domain: HEGEL, green+orange domain: FLUX.

Fig. 3 2D computational grid for flow field computations in Plasmatron X.

To include the magnetohydrodynamic effect of the coils on the flow, an overlapping domain of the torch section was created and simulated in FLUX. The grid used for FLUX along with the overlapping block in HEGEL are shown in Fig. 3e. Coupling between HEGEL and FLUX is done only in the torch volume sinceJoule heating and Lorentz force

distribution are concentrated near the coil region only.

C. Computational Domains for Material Response

To simulate the material response of the assembly, a structured 2-dimensional-axisymmetric wedge geometry was first meshed and simulated. As a simplification, the sample isoQ and the thermocouple plug are assumed to be the same body, in order to avoid skewing of mesh cells due to surface recession. 2D-axisymmetric meshes with increasing mesh resolution were created and used to perform mesh convergence studies to obtain a mesh that produces results with the optimum cell spacing and produces similar results as those from the finest mesh used. Using the optimal mesh spacing of the axisymmetric study, a 3-D-axisymmetric unstructured grid was built using Pointwise [18] to enable embedding thermocouples. Additional refinements were performed near the interfaces between materials and near the surface exposed to the aerothermal environment. The unstructured mesh was verified to produce the same results as the axisymmetric results.

U-shaped thermocouples (used in thermocouple plugs) and straight thermocouples of varying thicknesses at 15 mm depth from the stagnation point of the TPS sample were meshed. To simplify meshing in the thermocouple and avoid increasing skewness of the mesh, a square cross-section is assumed for the thermocouples. In order to mesh the thermocouples, line sources were created in the middle of the thermocouple wire and were used for scaling the cell sizes near the thermocouple. Through this method, uniformly varying cell sizes with minimal non-orthogonality were created. The minimum cell size was varied using the sources, between 1 and 5 cells in the thermocouple cross-section. To ensure adequate resolution while minimizing the skewness in the mesh, a cell size of 1.27×10^{-4} m, or 2 cells per thermocouple cross-section, was used. The meshes created for this study are shown in Fig. 4 with 30 and 24 American wire gauge (or 30-awg and 24-awg) thermocouples at 15 mm depth of the TPS sample.

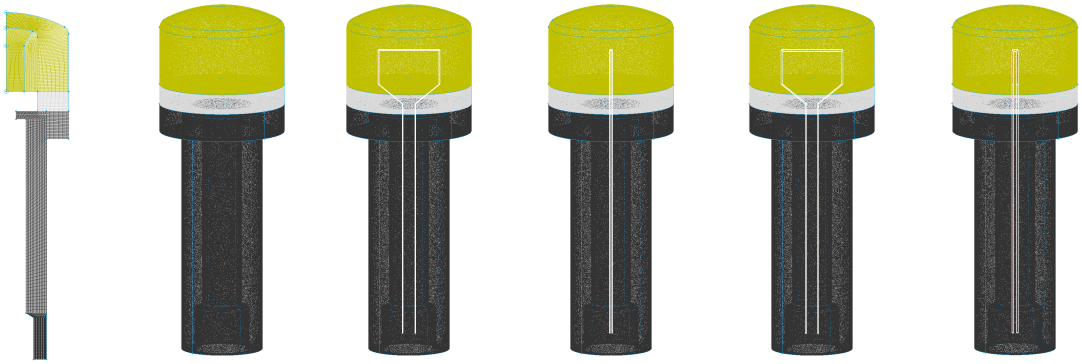

(a) Axisymmetric (b) 3D Unstructured (c) 30 awg U-shaped (d) 30 awg Straight (e) 24 awg U-shaped (f) 24 awg Straight

Fig. 4 Computational grids of the different assemblies used for material response simulations.

D. Boundary Conditions

The boundary conditions imposed for each of the flow and material domains are briefly described in this section. The numerical implementations of the flow boundary condition are elaborated in more details in Kumar et al.[19].

1. Fluid solver (HEGEL)

For HEGEL, the following boundary conditions are specified:

1) Inlet: Central injection at a mass flow rate of 0.86 g/s at an angle of 15° w.r.t vertical axis and a swirl angle of 24°. Sheath injection at a mass flow rate of 7.13 g/s horizontally into the chamber.
2) Outlet: subsonic outlet with a pressure of 1000 Pa
3) Walls and catch-cone: Cold-wall temperature of 300 K and no-slip boundary condition.
4) Sample Surface: Hot-wall temperature, based on previous experiments, of 2273 K at stagnation surface and 1473 K on the side of the sample. A cold-wall temperature of 300 K is assumed on the graphite stem. On all the surfaces, a no-slip boundary condition is applied.

2. Electromagnetic (FLUX)

The magnetic field solver (FLUX) is loosely-coupled with HEGEL, where coupling occurs every 100^{th} iteration of HEGEL and the coupled quantities remain frozen between successive coupling windows. The location and radius of the coils, operating radio frequency, and input power are provided to FLUX. For the 2D axi-symmetric computations performed in this work, the coils are assumed to be parallel and the current in the coils are modeled as point current sources which is a good assumption due to the skin-effect in the radio-frequency inductor coils. In future studies, accuracy of this assumption will be tested via 3D simulations where the actual coil cross-sections will be taken into account.

3. Material ressponse (PATO)

From the flow field obtained using the coupled framework, heat flux and pressure are interpolated along the surface, and are used as boundary conditions to PATO. The boundary layer edge along the stagnation line is identified as the inflection point in the gradient of the radial velocity with respect to the radial direction[20], and the enthalpy, velocity and density at the edge are computed. Using the boundary layer edge properties and the heat flux, the film-coefficient, $\rho_e u_e C_{H_0}$, is computed as,

$$\rho_e u_e C_{H_0} = \frac{q^{flow}}{(h_r - h_w)}, \tag{1}$$

where, h_r is the recovery enthalpy given by, $h_r = h_e + r u_e^2/2$, and $r \approx \sqrt{Pr} \approx 1$.

The Stanton number, C_{H_0}, is corrected for blowing correction due to pyrolysis gases blocking heat and mass transfer to the material. The blowing correction is given as,

$$C_H = C_{H_0} \frac{ln(1 + 2\lambda B')}{2\lambda B'} \tag{2}$$

Here, *B'* is a non-dimensional sum of mass fluxes due to pyrolysis gases and char ablation, and λ is a blowing correction taken as 0.4 to resemble a turbulent boundary layer. The *B'* solution procedure is used here at the stagnation surfaces for energy balance [21], and a blowing boundary condition was used for mass balance and surface recession assuming thermochemical equilibrium at the wall [22]. The inputs for *B'* are the species composition, Stanton number and enthalpy at the boundary layer edge, and the corrected film-coefficient. The Arbitrary Eulerian Lagrangian (ALE) approach is used for mesh motion due to recession of the material, where recession velocity is calculated using the *B'* approach.

Perfect contact is assumed in PATO between the numerous materials in the domain. The iso-Q dome is assumed to be porous and pyrolyzing, whereas the FBD insulator, graphite and thermocouples are assumed to be non-porous, heat conducting materials. In between the different materials, temperature and heat flux are imposed to be continuous. A zero-traction boundary condition is imposed for the pressure and zero mesh velocity from the dome to the insulator. Additionally, a radiative equilibrium boundary condition with imposed stagnation enthalpy and heat flux from the flow field for the faces of the insulator and graphite exposed to the flowfield. Finally, the temperature at the bottom of the assembly and bottom of the thermocouple leads was assumed to be the temperature of the water-cooled arm, 14°C, and an adiabatic wall boundary condition was imposed for the inner wall of the graphite holder.

E. Simulation Protocol and Test Matrix

For the aerothermal environment, a standard air plasma test was chosen, with an input power of 100 kW and a back-pressure of 1000 Pa. At an input power of 100 kW to the Plasmatron X facility, approximately 57.5 kW of power is supplied to the flow as computed by an energy balance for the facility. Non-local thermodynamic equilibrium (NLTE) simulations were performed at 57.5 kW power and 1000 Pa outlet pressure using an explicit RK4 time-integrator, and first and second order reconstructions procedures were used to compare the difference in results from both procedures. NLTE simulations in this work have been performed using Park 2T NLTE model[23] with air11 [e^-, N_2, O_2, NO, N, O, N_2^+, O_2^+, NO^+, N^+, O^+] kinetics.

Using the flow field boundary conditions, material response was performed for a few configurations of TPS materials and thermocouples. For the thermocouple simulations, numerous configurations with varying TPS material properties, thermocouple materials and thermocouple diameters were studied. The details of the parametric study conducted are detailed below:

1. Effect of Thermocouple Shape and Size

Firstly, the four configurations (30-awg U-shaped, 30-awg straight, 24-awg U-shaped, 24-awg straight) shown in Fig. 4 were simulated using Theoretical Ablative Composite for Open Testing (TACOT)[24, 25] as the TPS material, and Type K thermocouples. For TACOT with Type K thermocouples, the error produced due to varying size and shape of the thermocouple embedded into the TPS material is studied. From this study, the configuration producing the lowest error in temperature at the location of the thermocouple is obtained, and other parametric studies of varying thermocouple type and TPS material are conducted using this configuration.

2. Effect of Relative Material Properties

The relative thermal properties between TPS materials and thermocouple can have a significant effect on the error due to the presence of the thermocouple. To understand this behavior, three different ablating materials, TACOT, FiberForm and Graphite were simulated using the 30-awg U-shaped Type K thermocouple configuration. These three TPS materials were chosen to represent low-density porous pyrolyzing, low-density porous non-pyrolyzing, and high-density non-porous non-pyrolyzing materials, respectively. TACOT and Graphite are modeled as isotropic materials, whereas FiberForm is modeled as a transverse-isotropic material, with lower conductivity in the direction parallel to the flow.

3. Effect of Thermocouple Type

As different thermocouple types are made of different materials, the thermal conductivity, density and heat capacity of thermocouples can vary significantly. The commonly used thermocouples for high temperature applications are Type S, K and B. The properties used for these thermocouples, and their theoretical maximum temperatures are listed below in Table 1.

Table 1 Thermocouple properties used for simulations, taken from the Materials Handbook[26].

Type	Thermal Conductivity (W/m/K)	Specific Heat Capacity (J/kg/K)	Density (kg/m^3)	Thermal Diffusivity (m^2/s)	Maximum Temperature (°C)
K	25	450	8730	6.36×10^{-6}	1372
S	54.6	134	20700	1.49×10^{-5}	1768
B	38	134	19015	1.96×10^{-5}	1860

As these properties are significantly different between types of thermocouples, the error produced due to the presence of the thermocouple can vary. To study this behavior, TACOT is used as the TPS material and the thermocouple types are varied by specifying the respective material properties, and the error due the presence of each type of thermocouple is studied. In this study, as the thermocouple is simulated as a single wire, the average of the material properties of both leads were used as the effective material properties of the single thermocouple wire.

The overall test matrix of all the simulations performed is detailed in Table 2.

Table 2 Simulation test matrix.

Material	30 awg U-shaped	30 awg Straight	24 awg U-shaped	24 awg Straight
TACOT	Type K, S, B	Type K	Type K	Type K
FiberForm	Type K, S, B	Type K	Type K	Type K
Graphite	Type K, S, B	-	-	-

III. Results

A. Aerothermal Environment

First and second order NLTE simulations were performed for the Plasmatron X fluid domain. From the simulations, the heat flux and stagnation pressure at the surface of the test-sample are obtained, and are shown in Fig. 5 as a function of arc-length from the stagnation point of the sample. They are only shown for the top and side surface of the TPS and not for the graphite holder.

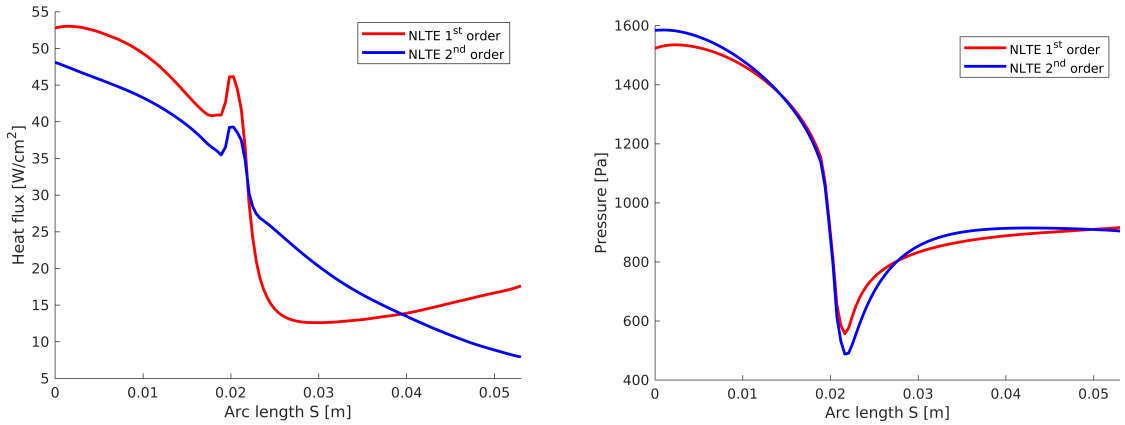

(a) Heat Flux (b) Stagnation Pressure

Fig. 5 Heat flux and stagnation pressure from NLTE simulations on the stagnation surface of the sample.

Fig. 5a shows that the peak heat flux estimated using NLTE is 50 W/cm^2. It can be seen that first order and second order reconstructions produced minimal variation in heat flux for the NLTE case. For obtaining boundary conditions for PATO simulations, the NLTE second-order reconstructed solution was used.

Using the simulation results, the gradient of the velocity field was computed using finite-difference and the gradient of radial velocity (v) in the y direction, or $\frac{\partial v}{\partial y}$, was computed along the stagnation line. The inflection point of this derivative along the axial direction, where $\frac{\partial^2 v}{\partial x \partial y} = 0$, was considered the boundary layer edge. Fig. 6 shows the variation of these quantities close to the stagnation point.

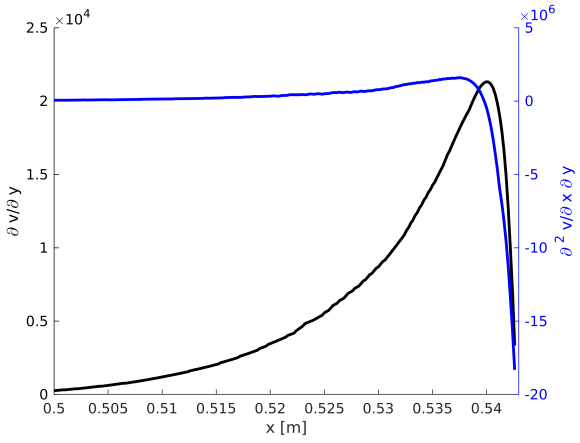

Fig. 6 Profile of $\frac{\partial v}{\partial y}$ along the stagnation line, and its derivative w.r.t the axial direction, used for identifying the boundary layer edge.

From Fig. 6, the boundary layer edge was identified for the simulation, producing a boundary layer thicknesses of

3 mm from the stagnation point, respectively. Therefore, the edge enthalpy and species composition were identified using the location determined from Fig. 6. The overall boundary conditions obtained for the chosen power and pressure are presented in Table 3.

Table 3 Boundary conditions for PATO simulations, obtained from the aerothermal environment.

h_e (MJ/kg)	h_{wall} (MJ/kg)	$\rho_e u_e C_{H_0}$ (-)	p_{wall} (Pa)
20.4	9.6	0.045	1584.3

B. Material Response

Material response simulations were performed in PATO using the stagnation heat flux and pressure along with boundary layer edge properties for the geometries shown in Fig. 4. Firstly, simulations without thermocouples were conducted and used as a reference solution for comparing the effect of different embedded thermocouples. The results obtained for each parametric study are presented in this section.

1. Effect of Thermocouple Shape and Size

For the four different thermocouple configurations shown in Fig. 4, PATO simulations were performed using TACOT as the TPS material and a Type K thermocouple at 15 mm depth from the stagnation surface of the TPS sample. The temperature contours at a slice in the middle are shown for the cases simulated, at a time of 30 seconds when the sample is at the highest temperature.

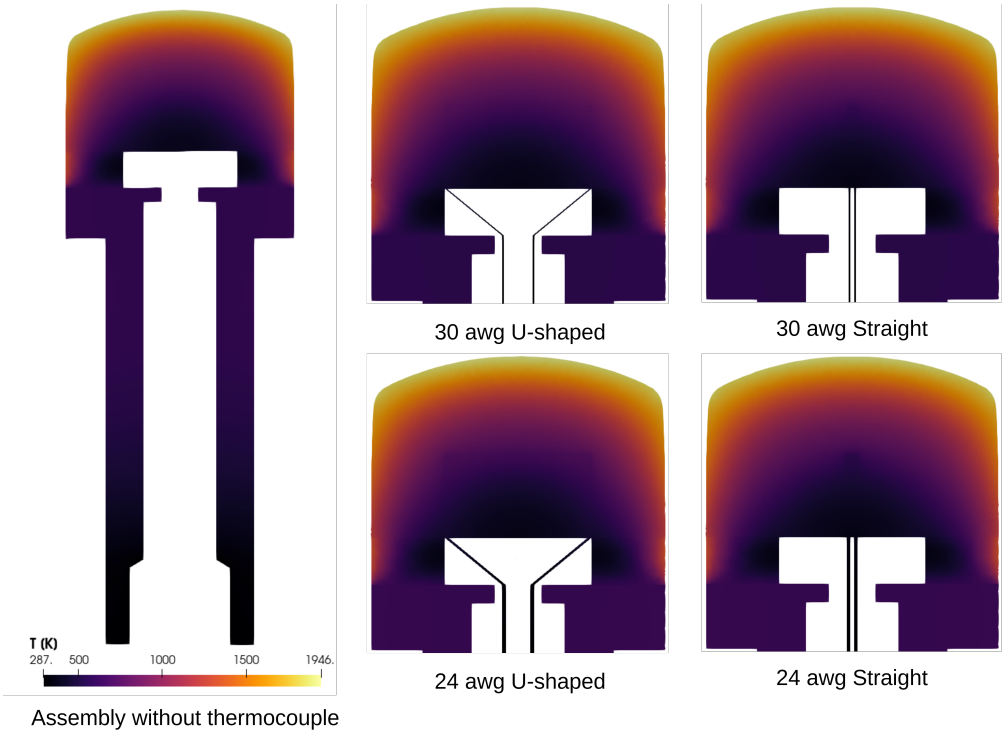

Fig. 7 Temperature contours for a vertical slice of the assembly at t = 30 seconds.

Fig. 8a shows the temperature profiles at the top, 5 mm, 10 mm and 15 mm depth, and bottom of the TPS sample. The deviation in temperature at a depth of 15 mm for these cases indicates the effect of the physical presence of the thermocouple and its leads being at a cooler temperature of 14°C. The error in temperature at 15 mm depth due to the presence of a thermocouple with respect to the temperature at the same location without a thermocouple is shown in Fig.

8b.

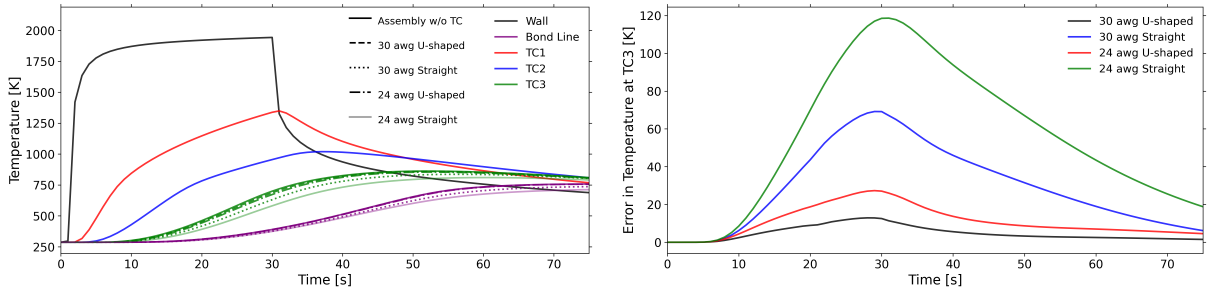

(a) Temperature Profiles

(b) Error in Temperatures

Fig. 8 (a) Temperature profiles at the wall, bottom and thermocouple locations of the TPS sample, (b) Error in temperature with respect to the temperature without a thermocouple at 15 mm depth.

Fig. 8a shows that the temperature at the top, 5 mm, 10 mm depth are unaffected by the presence of the thermocouple. However, the temperature at 15 mm depth of the sample is different for all the cases, indicating that the physical presence of the thermocouple changes the temperature locally at this location. With the 30 awg U-shaped thermocouple, the temperature at the 15 mm depth is slightly lower, with a maximum difference of 12.9°C or 1.96%, compared to the temperature without a thermocouple. On the other hand, the temperature profile for the 30 awg straight thermocouple has a much higher deviation compared to the 3D-axisymmetric case with a maximum difference of 69.2°C or 10.19%. Varying the size, of the thermocouple to 24 awg also causes the error in temperature to increase. The U-shaped 24 awg produces an error in temperature of 27.3°C or 4.02%, whereas the 24 awg straight thermocouple produces a much higher error of 118.6°C or 16.5%.

Additionally, from Fig. 8b, it can be seen that the error increases with time while the assembly is heated by the flow. Once the heating is stopped, the temperature in the TC3 location is seen to level off and gradually decrease. This causes the error in the thermocouple measurement to reduce. Therefore, the error due to the presence of the thermocouple is highest in the transient heating stage and eventually diminishes to a steady state, non-zero error. This study showed that using thermocouples with a thinner gauge reduces the intrusive effects on temperature. Moreover, the way the thermocouple is embedded into the sample also has a significant effect on the temperature, with the U-shaped thermocouple performing much better than the straight thermocouple for any given gauge. This result is consistent with findings from literature[4, 5] that reported that placing the thermocouple lead wires parallel to the heat flow (straight thermocouple in this case) produced much larger errors compared to if the lead wires were placed perpendicular to the heat flow (U-shaped in this case). It is concluded that a 30 awg U-shaped thermocouple is ideal as it minimally alters the local material temperature.

2. Effect of Material Properties

Using the Type K 30 awg U-shaped thermocouple configuration, TACOT, FiberForm and Graphite ablation were simulated. The temperature profiles for the different materials at the top and 15 mm depth are shown in Fig. 9a. The error in temperature at 15 mm depth with and without a thermocouple is shown in Fig. 9b.

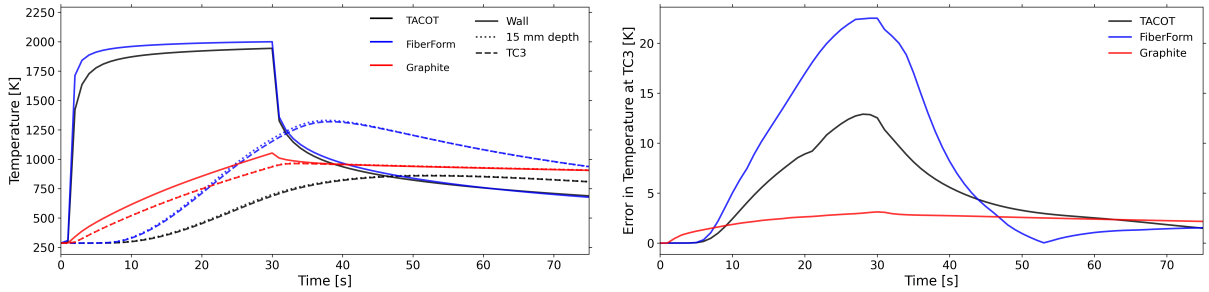

(a) Temperature Profiles

(b) Error in Temperatures

Fig. 9 (a) Temperature profiles at the wall and thermocouple locations of the TPS sample, (b) Error in temperature at 15 mm depth with respect to the temperature without a thermocouple, for TACOT, FiberForm and Graphite.

From Fig. 9a, it can be seen that the temperature on the wall and within the sample are different for the three materials simulated. The temperatures are much higher in the case of FiberForm when compared to TACOT or Graphite. Due to this difference in temperature at the TC3 location, the errors due to the presence of the thermocouple are also different for these materials.

Fig. 9b shows that the error in temperature is the highest for FiberForm, with a maximum error of 22.5°C (1.98%) compared to TACOT with a maximum error of 12.9°C (1.96%). However, it should be noted that the percent error in temperature are identical for TACOT and FiberForm, as the thermal conductivity, density and heat capacity of the two materials are of similar order of magnitude. Conversely, though Graphite has a much higher temperature at TC3 than TACOT, the error is much lower for Graphite as the thermal conductivity and heat capacity of graphite are much higher than those of TACOT, and comparatively closer to those of the Type K thermocouple. Therefore, it can be concluded that the error due to the thermocouple's presence is dependent on the relative material properties of the TPS material and the thermocouple.

3. Effect of Thermocouple Type

For the 30 awg U-shaped thermocouple configuration, the type of thermocouple was varied between Types S, K and B using TACOT as the TPS material. Using the same boundary conditions from §III.A, material response simulations were performed, and the error in temperature at 15 mm depth is compared. The error is shown in Fig. 10a.

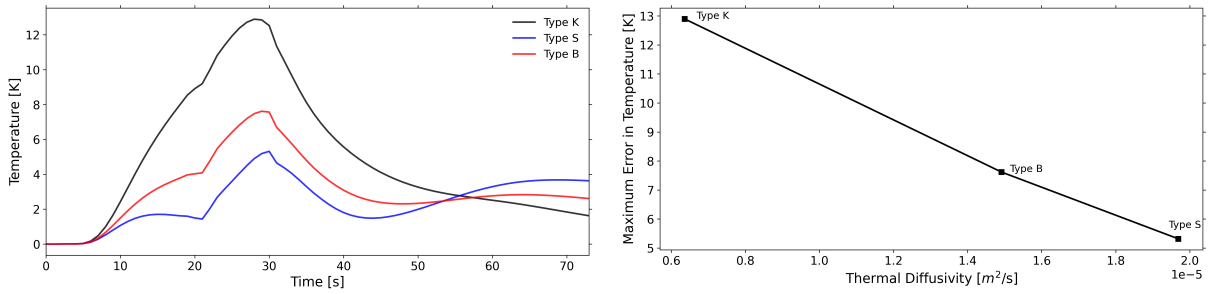

(a) Error in Temperatures

(b) Maximum error vs. thermal diffusivity

Fig. 10 (a) Error in temperature at 15 mm depth for different thermocouple types with the 30 awg U-shaped configuration, (b) Maximum error due to thermocouples as a function of thermal diffusivity of the thermocouple type.

The error due the thermocouple presence is seen to vary with the type of thermocouple, with the lowest error produced for the Type S thermocouple, followed by Type B, and Type K producing the largest error. As the only parameters varied for simulating the different thermocouple types were the material properties of each type, the variation

of the error was compared with the thermal diffusivity, $\alpha = \frac{k}{\rho C_p}$ of the thermocouple types. The error as a function of the material diffusivity of the thermocouples is shown in Fig. 10b, with a linear decrease in the maximum error as the diffusivity of the thermocouple increased. Therefore, this study showed that thermocouples with high thermal diffusivity act as the least intrusive materials when embedded into the TPS material, and are ideal for temperature measurements in TPS samples.

To further observe the influence of relative material properties of the TPS material and the thermocouple, FiberForm and Graphite were simulated using the 30 awg U-shaped configuration with the 3 types of thermocouple materials. The maximum error as a function of thermal diffusivity of the thermocouples is shown in Fig. 11.

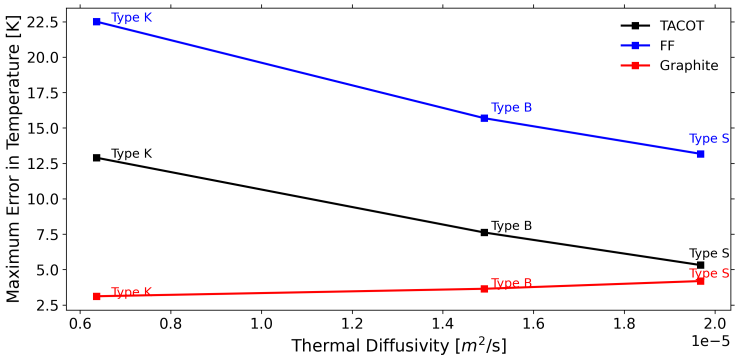

Fig. 11 Maximum error due to thermocouples as a function of thermal diffusivity of the thermocouple type for TACOT, FiberForm and Graphite as the TPS material.

It can be seen that the maximum error for FiberForm decreases with increasing thermal diffusivity of the thermocouple, similar to the trend seen for TACOT. For Graphite, the error is seen to be minimal for all the cases but slightly increasing with increasing diffusivity.

4. Augmented Heating due to Thermocouple Presence

For the 30 awg U-shaped thermocouple, as the two wires are closer to the side-walls of the TPS sample, the depth of the wire might be closer to the side than from the stagnation point. In such conditions, the temperature on the edges of the thermocouple could be higher than the temperature at the junction, and as the thermocouple wire has a high thermal diffusivity, this could in turn lead to the thermocouple junction getting hotter and measuring a higher temperature than the temperature at that location without a thermocouple. This phenomenon can also be observed if the TPS material is preferentially oriented and there is a significant difference in material properties in different directions. This behavior was observed while simulating the FiberForm studies with different type of thermocouples. The error in temperature at 15 mm depth as a function of time is shown in Fig. 12.

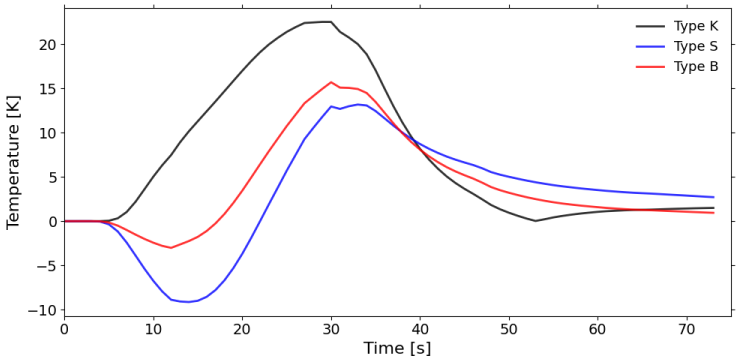

Fig. 12 Error in temperature at 15 mm depth due to presence of different types of thermocouples, using FiberForm as the TPS material and 30 awg U-shaped thermocouple configuration.

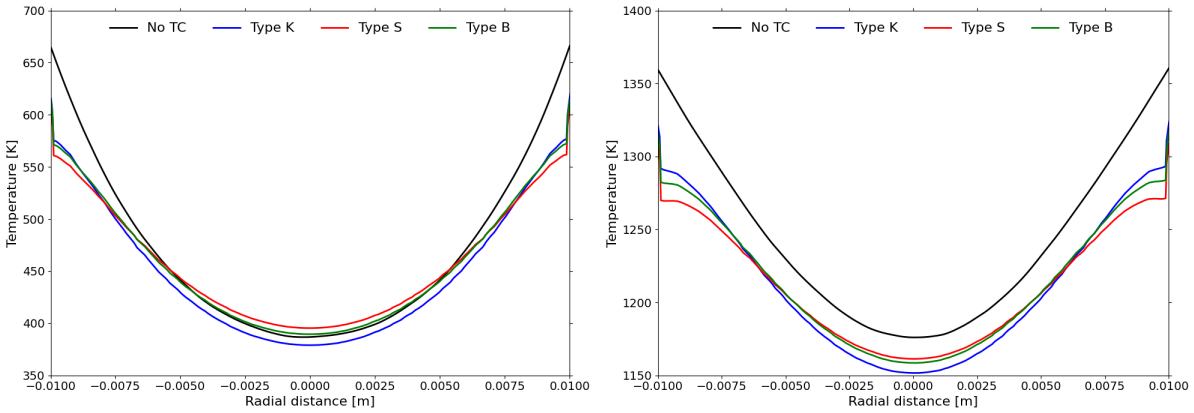

(a) t = 12 seconds

(b) t = 30 seconds

Fig. 13 Temperature profile at 15 mm depth along the length of the thermocouple for a simulation time of (a) t = 12 seconds, and (b) t = 30 seconds.

From Fig. 12, it can be seen that the error in temperature first is negative for Types S and B thermocouples, indicating that the temperature is higher at 15 mm depth with the thermocouple than without. This is due to the transverse-isotropic properties used for simulating FiberForm, and due to the proximity of the thermocouple wires to the side of the sample. As the sample is heated on the side and the thermal conductivity is higher in the side wise direction, the temperature at the edge of the thermocouple is higher, augmenting heating on the thermocouple junction itself initially. However, as the temperature at the stagnation point increases and the heat conducts to the thermocouple junction, the temperature at the junction increases. It can also be noted that this negative error does not arise for the Type K thermocouple due to its lower thermal diffusivity. The temperature profile at 15 mm depth along the length of the thermocouples is shown in Fig. 13 at the simulation times of 12 seconds and 30 seconds, where the error is maximum as seen in Fig. 12.

The temperature profile at 12 seconds clearly show that the sides of the thermocouple are always hotter than the junction at the center, and that the temperature at the edge of thermocouple is much lower than the temperature without a thermocouple. However, it can also be seen that for the Type S and B thermocouples, the temperature at the junction of the thermocouple is higher than that without a thermocouple, showing the adverse effect of heating of the thermocouple junction from the sides. As the sample is further heated for up to 30 seconds, the temperature in the entire sample increases, and the effect of heating of the thermocouple from the side decreases, causing it to produce the anticipated effect of lower temperature at the junction than the temperature without a thermocouple.

Therefore, this preliminary analysis of the thermocouple adversely heating the sample showed that the proximity of the thermocouple wire to the sides of the sample could cause temperature measurements to be higher in some cases when compared the temperature without a thermocouple. This effect was however seen to be mild in this case due to a large enough distance of 50% radius from the thermocouple wire to the side walls. For general purposes of instrumenting samples with thermocouples, such a study could be considered in determining ideal thermocouple plug size for experiments that would produce minimal error due to side-wall heating effects. Additionally, as placing the thermocouple junction perfectly in the middle of the sample is practically challenging, the junction is often slightly offset. From Fig. 13, it can be seen that offsetting the junction slightly can cause much higher errors in temperature, of up to 100°C in this case for the Type S thermocouple.

5. Overall Results

The maximum error obtained for each thermocouple configuration are tabulated in Table 4. The table includes the different TPS materials studied and thermocouple types that were considered.

IV. Conclusion & Future Work

In this paper, the necessities of performing high-fidelity material response simulations of test assemblies to characterize TPS materials have been addressed. The coupled multi-physics framework developed at UIUC was used

Table 4 Maximum error in temperature at the thermocouple location.

Material	30- awg U-shaped	30 awg Straight	24 awg U-shaped	24 awg Straight
TACOT	Type K: 12.9°C (1.96%) Type S: 5.3°C (0.75%) Type B: 7.6°C (1.12%)	69.2°C (10.19%)	27.3°C (4.02%)	118.6°C (16.50%)
FiberForm	Type K: 22.5°C (1.98%) Type S: 15.7°C (1.04%) Type B: 13.2°C (1.34%)	95.6°C (9.41%)	45.94°C (4.18%)	175.58°C (16.57%)
Graphite	Type K: 3.1°C (0.33%) Type S: 3.6°C (0.39%) Type B: 4.2°C (0.45%)	-	-	-

for simulating the aerothermal environment of the Plasmatron X, and details for obtaining boundary conditions for flow around TPS samples were described. These boundary conditions were used to simulate the material response in PATO for an isoQ geometry using TACOT properties [27] with and without embedded thermocouples. Comparing the temperature at 15 mm depth from the stagnation point at the surface, with and without a physical thermocouple showed significant differences based on the configuration of thermocouple that was embedded. It was observed that using a 30 awg U-shaped Type K thermocouple produced the most optimal result, with minimal variation in temperature at the 15 mm depth location. We find that increasing the size, or gauge, of the thermocouple increased the error, due to the thermocouple acting as a large heat sink reducing the temperature locally. The way the thermocouples are embedded into the TPS material was also seen to have drastic effects, with the U-shaped thermocouple performing significantly better than the straight thermocouple.

Further parametric studies with varying the thermocouple type using the 30 awg U-shaped configuration showed that the type of thermocouple also contributed to the error in temperature at the thermocouple location. It was observed that the error reduced with increasing diffusivity of the thermocouple, thereby showing that selecting the type of thermocouple correctly is also crucial for accurate temperature measurements in high-enthalpy material testing. Finally, varying the TPS material itself varied the error in temperature at the thermocouple location. The error was found to be highest for FiberForm, followed by TACOT and then Graphite. This error was seen to be a function of relative properties between the TPS material and the thermocouple type.

In conclusion, this paper showed that assembly components and thermocouple presence can skew the results of high-enthalpy testing of instrumented material assemblies. The error due to thermocouples was found to be a function of size, shape, material properties of the thermocouples and also a function of the properties of the TPS materials, indicating that these factors need to be considered while planning for high-enthalpy testing of instrumented test articles. This study also showed that to accuratly simulate material response of thermocouple plugs in arc-jets, inductively coupled plasma facilities and even real atmospheric entry scenarios, the secondary components used to assemble the test articles and all embedded features must be included. Future work in this project will include simulating multiple thermocouples in a single assembly, experimenting with this chosen assembly in the Plasmatron X and comparing with simulation results.

Acknowledgements

This work was supported by NASA Space Technology Graduate Research Opportunity Grant 80NSSCC22K1192, and the Center for Hypersonics & Entry Systems Studies (CHESS) at the University of Illinois at Urbana-Champaign. The authors thank Dr. Sung Min Jo, Prathamesh Sirmalla, Benjamin Ringel, and our colleagues at CHESS for their guidance with this work. We would also like to thank Jeremie Meurisse and the Predictive Material Modeling Team at NASA Ames, and Jeff Engerer at Sandia National Laboratories.

References

[1] Duffa, G., *Ablative thermal protection systems modeling*, American Institute of Aeronautics and Astronautics, Inc., 2013.

[2] Chazot, O., and Panerai, F., "High-enthalpy facilities and plasma wind tunnels for aerothermodynamics ground testing," 2015.

[3] Bottin, B., Chazot, O., Carbonaro, M., Van Der Haagen, V., and Paris, S., "Measurement techniques for high enthalpy and plasma flows," Tech. rep., RTO-EN, 2000.

[4] Brewer, W. D., "Effect of thermocouple wire size and configuration on internal temperature measurements in a charring Ablator," Tech. rep., 1967.

[5] Dow, M. B., *Comparison of measurements of internal temperatures in ablation material by various thermocouple configurations*, National Aeronautics and Space Administration, 1964.

[6] Capponi, L., Oldham, T., Konnik, M. T., Stephani, K., Bodony, D. J., Panesi, M., Elliot, G. S., and Panerai, F., "Aerothermal characterization of the Plasmatron X Wind Tunnel: Heat flux, Stagnation Pressure and Jet Unsteadiness," *AIAA SCITECH 2023 Forum*, 2023.

[7] Oldham, T., Capponi, L., Konnik, M., Stephani, K., Bodony, D. J., Panesi, M., Elliott, G. S., and Panerai, F., "Aerothermal Characterization of the Plasmatron X Wind Tunnel: Optical Emission Spectroscopy and Jet Temperature Reconstruction," *AIAA SCITECH 2023 Forum*, 2023, p. 2516.

[8] Munafò, A., Chiodi, R., Kumar, S., Le Maout, V., Stephani, K. A., Panerai, F., Bodony, D. J., and Panesi, M., "A Multi-Physics Modeling Framework for Inductively Coupled Plasma Wind Tunnels," *AIAA SCITECH 2022 Forum*, 2022, p. 1011.

[9] Munafò, A., Alberti, A., Pantano, C., Freund, J. B., and Panesi, M., "A computational model for nanosecond pulse laser-plasma interactions," *Journal of Computational Physics*, Vol. 406, 2020, p. 109190.

[10] Kumar, S., Munafò, A., Jo, S. M., Mansour, N. N., and Panesi, M., "High-fidelity simulation of RF inductively coupled plasma discharges," *AIAA AVIATION 2022 Forum*, 2022, p. 3362.

[11] Kumar, S., Munafò, A., Le Maout, V., Mansour, N., and Panesi, M., "Self-consistent magneto-hydrodynamic modeling of ICP discharges," *AIAA SCITECH 2022 Forum*, 2022, p. 1619.

[12] Bungartz, H.-J., Lindner, F., Gatzhammer, B., Mehl, M., Scheufele, K., Shukaev, A., and Uekermann, B., "preCICE–a fully parallel library for multi-physics surface coupling," *Computers & Fluids*, Vol. 141, 2016, pp. 250–258.

[13] Jo, S. M., Kumar, S., Le Maout, V., Munafò, A., and Panesi, M., "Multi-Fidelity Modeling Framework for Radiative Transfer in Hypersonic Atmospheric Entry," *AIAA SCITECH 2023 Forum*, 2023, p. 1730.

[14] Lachaud, J., and Mansour, N. N., "Porous-material analysis toolbox based on OpenFOAM and applications," *Journal of Thermophysics and Heat Transfer*, Vol. 28, No. 2, 2014, pp. 191–202.

[15] Milos, F. S., and Chen, Y.-K., "Ablation and thermal response property model validation for phenolic impregnated carbon ablator," *Journal of Spacecraft and Rockets*, Vol. 47, No. 5, 2010, pp. 786–805.

[16] Gazarik, M. J., Wright, M. J., Little, A., Cheatwood, F. M., Herath, J. A., Munk, M. M., Novak, F. J., and Martinez, E. R., "Overview of the MEDLI Project," *2008 IEEE Aerospace Conference*, IEEE, 2008, pp. 1–12.

[17] Ventura Diaz, P., Yoon, S., Panerai, F., and Mansour, N. N., "Simulation of hymets flowfield around baby-sprite entry probe," *AIAA Aviation 2019 Forum*, 2019, p. 3262.

[18] Karman, S. L., and Wyman, N. J., "Automatic unstructured mesh generation with geometry attribution," *AIAA Scitech 2019 Forum*, 2019, p. 1721.

[19] Kumar, S., Jo, S. M., Munafo, A., Bodony, D. J., and Panesi, M., "Numerical study of radiative heat effects in inductively coupled plasma discharges," *Submitted to AIAA AVIATION 2023 Forum, San Diego CA, 12-16 June*, 2023.

[20] Barbante, P. F., Degrez, G., and Sarma, G., "Computation of nonequilibrium high-temperature axisymmetric boundary-layer flows," *Journal of thermophysics and heat transfer*, Vol. 16, No. 4, 2002, pp. 490–497.

[21] Chen, Y.-K., and Milos, F. S., "Ablation and thermal response program for spacecraft heatshield analysis," *Journal of Spacecraft and Rockets*, Vol. 36, No. 3, 1999, pp. 475–483.

[22] Wool, M. R., "Aerotherm equilibrium surface thermochemistry computer program, version 3. volume 1. program description and sample problems," Tech. rep., AEROTHERM CORP MOUNTAIN VIEW CA, 1970.

[23] Park, C., Jaffe, R. L., and Partridge, H., "Chemical-kinetic parameters of hyperbolic earth entry," *Journal of Thermophysics and Heat transfer*, Vol. 15, No. 1, 2001, pp. 76–90.

[24] Lachaud, J., Martin, A., Cozmuta, I., and Laub, B., "Ablation workshop test case," *4th Ablation Workshop*, 2011, pp. 1–3.

[25] Lachaud, J. R., Martin, A., van Eekelen, T., and Cozmuta, I., "Ablation Test-Case Series# 2. Numerical Simulation of Ablative-Material Response: Code and Model Comparisons," 2012.

[26] Cardarelli, F., "Materials handbook: a concise desktop reference," 2008.

[27] Lachaud, J., van Eekelen, T., Scoggins, J. B., Magin, T. E., and Mansour, N. N., "Detailed chemical equilibrium model for porous ablative materials," *International Journal of Heat and Mass Transfer*, Vol. 90, 2015, pp. 1034–1045.